Volume 4
Number 11
7 June 2023
Pages 2395–2514

Materials Advances

rsc.li/materials-advances

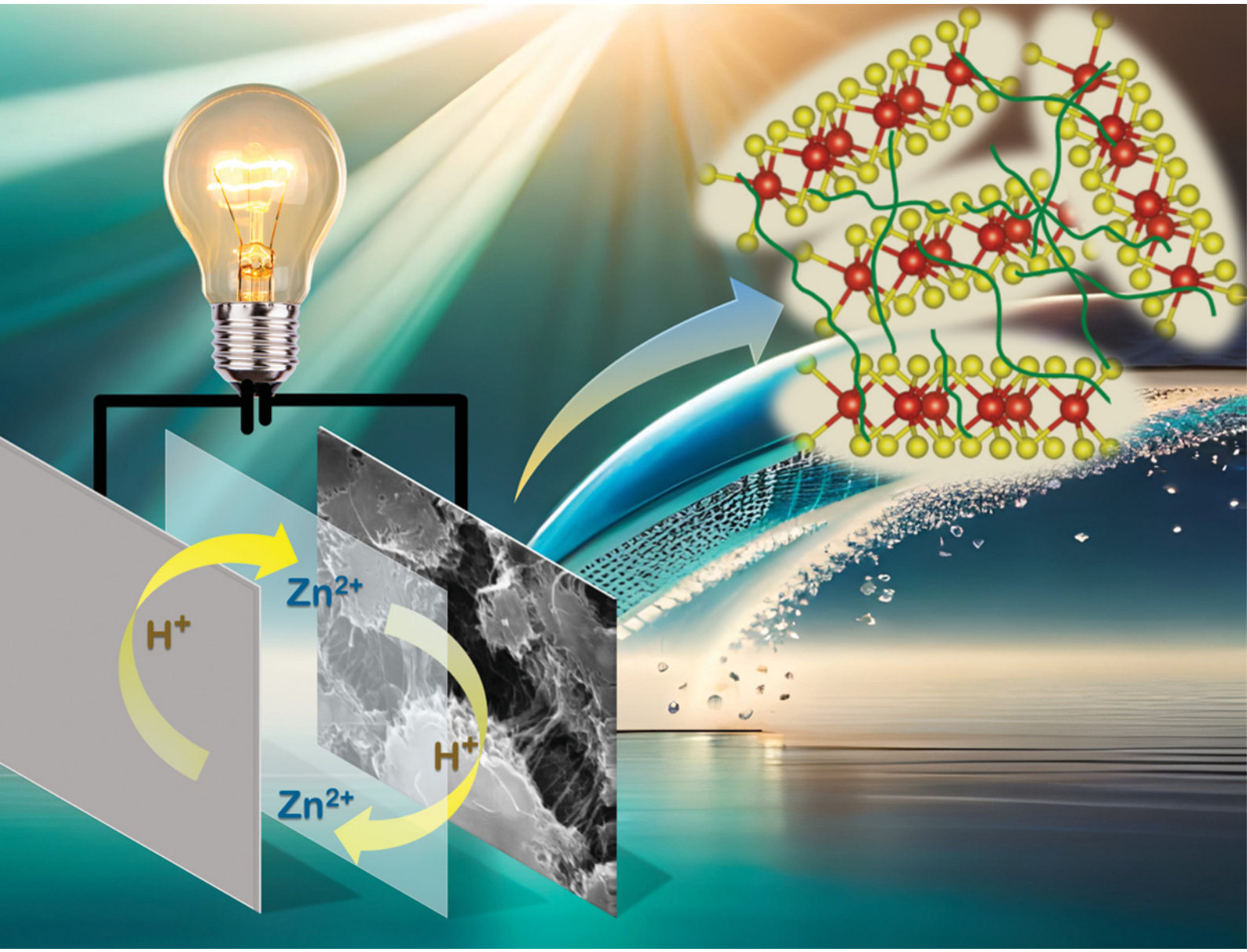

ISSN 2633-5409

ROYAL SOCIETY OF CHEMISTRY

PAPER

Santosh K. Singh, Bimlesh Lochab *et al.*
Nano-wired polyaniline/VS_2 composite materials for quasi-solid-state supercapacitor and zinc-ion battery applications

Materials Advances

ROYAL SOCIETY OF CHEMISTRY

PAPER

View Article Online
View Journal | View Issue

Cite this: *Mater. Adv.*, 2023, 4, 2425

Nano-wired polyaniline/VS_2 composite materials for quasi-solid-state supercapacitor and zinc-ion battery applications†

Saad Zafar,[a] Santosh K. Singh*[b] and Bimlesh Lochab *[a]

Electrochemical energy storage devices, including supercapacitors and metal-ion batteries, are some of the most sustainable energy technologies. The advancement of layered materials constantly improves the charge storage capacity of these devices by facilitating the intercalation/de-intercalation mechanism. In the present study, we have prepared a PANI/VS_2 composite material using a facile method and used it to fabricate quasi-solid-state supercapacitors (QSSCs) and zinc ion batteries (ZIBs). *In situ* growth of PANI on the layered VS_2 improved the conductivity and charge acceptor sites during the cycling process. The PANI/VS_2 composite showed an specific capacitance of 822 F g^{-1} at 2 A g^{-1} discharge current density due to the pseudocapacitance contribution from PANI. In addition, the observed nanowire network of PANI over the VS_2 surface facilitated the electrolyte accessibility. The assembled ZIB, with PANI/VS_2 as the cathode, showed a charge storage capacity of 219 mA h g^{-1} at a discharge rate of 0.1 A g^{-1} with a coulombic efficiency of ~100% after 750 continuous cycles at 3 A g^{-1}. The observed higher charge storage capacity and the cycling reversibility of the devices are attributed to the robustness of the prepared PANI/VS_2 composite material.

Received 14th February 2023,
Accepted 14th April 2023

DOI: 10.1039/d3ma00070b

rsc.li/materials-advances

1. Introduction

The sustained exploitation of fossil fuel-based energy largely affects the environment, which urges the development of green and clean energy technologies. The invention of electrochemical energy conversion (fuel cells, electrolyzers, and redox flow batteries) and storage (metal-ion batteries and supercapacitors) devices greatly affects the global lifestyle.[1] Among these energy technologies, Li-ion batteries are considered the most evolved energy storage devices because of their usability and high performance.[2] The growing overdependence on existing natural reserves and the high reactivity of Li metal towards air and moisture have raised economic and safety concerns.[3] In contrast, aqueous electrochemical energy devices such as aqueous supercapacitors and metal-ion batteries are more economical and avoid complications of battery operation under moisture-free conditions.[4] However, the narrow operational potential window and rechargeability of aqueous energy storage devices remain challenging. Therefore, considerable efforts are being made toward developing high-performance electrode materials to increase energy and power density.[5]

In recent years, supercapacitors (SCs) have attracted considerable attention due to their fast charge–discharge rates, high power density, and long cycle lifetime. However, issues of low energy density ascribed to their different energy-storage mechanisms still hinder their practical applications.[6] Compared to supercapacitors the aqueous rechargeable metal-ion batteries conceives better charge storage capacity owing to the reversible shuttling of metal ions such as Zn^{2+} in zinc-ion batteries (ZIBs).[7] The abundant availability of zinc naturally and its lower reduction potential of −0.78 V *vs.* SHE enable zinc to be an attractive anode material for aqueous metal-ion batteries.[8,9] Considering the importance of the electrode materials in SC and ZIB cathodes, the development of a high-surface area materials with improved conductivity is of high priority.[9] Advancements in porous carbon materials and transition metal oxides led to improved intercalation of metal ions, increasing the overall storage capacity output.[10,11] However, the achieved charge storage capacity is still far from realizing the theoretical capacity offered by the SCs and ZIBs. Thus, exploring layered and stable materials as charged ion acceptors is one of the best methods for these applications.

Layered transition-metal dichalcogenides (TMDs), such as MoS_2, WS_2, and VS_2, have received significant attention in

[a] *Materials Chemistry Laboratory, Department of Chemistry, School of Natural Sciences, Shiv Nadar Institution of Eminence, Delhi-NCR-201314, India. E-mail: bimlesh.lochab@snu.edu.in*
[b] *Electrochemical-Energy Laboratory, Department of Chemistry, School of Natural Sciences, Shiv Nadar Institution of Eminence, Delhi-NCR-201314, India. E-mail: santosh.singh1@snu.edu.in*

† Electronic supplementary information (ESI) available. See DOI: https://doi.org/10.1039/d3ma00070b

various applications due to their outstanding characteristics.[11–14] TMDs possess a graphene-like layered structure with a direct bandgap, which facilitates fast ion diffusion. The associated properties of TMDs enable them to be a potential electrode material for electrochemical energy applications. TMD-based electrodes showed excellent activity towards SCs and Li/Na-ion batteries.[12,14,15] This class of materials also showed great potential for the insertion/extraction of multivalent ions (Zn^{2+}, Mg^{2+}, and Al^{3+}) owing to the characteristic of large interlayer spacing.[16,17] VS_2 is a hexagonal system, and shows a similar crystal structure to that of graphite with an interlayer spacing of 5.76 Å, in which the vanadium layer lies between two sulfur layers forming a sandwich structure.[14,18] In the VS_2 crystal structure, each V atom is arranged around six S atoms *via* covalent connections. The large interlayer spacing of VS_2 enables ease of insertion/extraction of lithium ions (0.69 Å), sodium ions (1.02 Å), and zinc ions (0.74 Å) as such, or as solvated ions in an aqueous electrolyte. However, the lower conductivity of VS_2 compared to that of graphitic carbon materials has limited its applicability in energy storage devices.

The conductivity of VS_2 layered materials can be improved by adding conducting additives such as carbon and conducting polymers.[19,20] In this study, polyaniline (PANI) nanofibers are grown over VS_2 layers, and the resulting composite was used as an active material with improved overall conductivity.

Wang *et al.*[21] reported the capacitance of layered VS_2 as 105 F g^{-1}, while VS_2 was prepared using a solvothermal method, followed by layer separation achieved by the sonication method. The capacitance reported for the layer-separated VS_2 materials was mainly contributed by the electrical double-layer capacitance (EDLC). The observed value is lower than most of the carbon-based layered conducting materials. PANI/VS_2 composite materials are not well explored for electrochemical energy storage devices in the literature. Furthermore, studies are limited to only a 3-electrode set-up using liquid electrolytes, far from the real-time application of the electrode materials in quasi-solid-state supercapacitor devices. The prepared PANI/VS_2 composite electrode in SCs can store energy by ion adsorption and a surface redox reaction, as in double-layer capacitors and pseudocapacitors. Incorporating PANI into the layered VS_2 offers several advantages over other pseudocapacitive materials, such as high theoretical capacitance, flexibility to alter its chemical and structural properties, and cost-effectiveness.[20] Bulk PANI interacts with electrolytes inadequately and thus increases the inactive surface area available for the electrochemical reactions, thus leading to reduced specific capacitance. Alternatively, controlled polymerization of aniline over layered VS_2 surfaces may form interconnected channels, enhancing ion transport and accessibility within VS_2 layers and PANI, eventually boosting the overall capacitance.[22]

Likewise, the high storage capacity of ZIBs is hampered due to the relatively large hydration and high polarization of bivalent zinc ions leading to sluggish diffusion kinetics and is considered one of the major challenges to meet the commercial requirements. The poor mobility and accessibility of the cathode materials are desired to mitigate some of these issues, in particular, the limited accessibility of Zn^{2+} ions to the stacked VS_2 layers, the lack of ion acceptors at the cathode, and the low energy density of ZIBs. Recently, Fu *et al.*[23] reported a highly reversible ZIB by employing PANI as the cathode material with >99.9% coulombic efficiency. However, the typical interfacial parasitic activity, hydrogen evolution reaction (HER), and corrosion, associated with the use of an aqueous electrolyte during charge–discharge cycles, are observed. In ZIBs, the H^+ and Zn^{2+} ion insertion kinetics in the cathode primarily depends on the components, crystallographic polymorphs, and the particle size of the active materials.[24] Studies showed that the insertion of H^+ ions improves the ZIB performance and facilitates the Zn^{2+} ion mobility. To improve the H^+ ion insertion, employing a proton conducting Nafion® membrane as a separator can facilitate the efficient ion transport.[25] In addition, pseudocapacitive faradaic processes are also an important factor in enhancing the charge storage capacity and rate capability of the batteries. Therefore, adding PANI to the layered VS_2 electrode materials may improve the fast charge transfer kinetics and rate capability. It is well understood that the >C═O and N–H functional groups present in the cathode materials can accept and accommodate high Zn^{2+} amounts and allow reversibility, thus improving the overall cyclability of the batteries.

Understanding the advantages of VS_2 and PANI as electrode materials, we have synthesized a PANI/VS_2 composite, which has shown a remarkable performance in a quasi-solid-state supercapacitor (QSSC) and ZIB. The fabricated QSSC and ZIB showed a charge storage capacity of 822 F g^{-1} at 2 A g^{-1} and 219 mA h g^{-1} at 0.1 A g^{-1} discharge rate. The PANI/VS_2 composite-based fabricated devices displayed enhanced performance compared to the pristine VS_2 and PANI alone, showcasing the importance of the layered structure of VS_2 and the conducting PANI.

2. Results and discussion

2.1. Physical characterization

The synthesis of PANI/VS_2 composite materials and fabrication of QSSC and ZIB devices are shown schematically in Scheme 1. A detailed discussion of the synthesis and device fabrication process is presented in the Experimental section.

The field-emission scanning electron microscopy (FESEM) images of pristine PANI (Fig. 1(a) and (b)) showed agglomerated structures resulting from the bulk polymerization of aniline monomers, restricting the accessibility of electrolyte ions. In contrast, pristine VS_2 showed 3-dimensional nanoflakes with relatively porous morphology (Fig. 1(c) and (d)), which may enable an active scaffold and provide a large surface area to form the PANI/VS_2 composite. Fig. 1(e) and (f) displays the FESEM images of PANI/VS_2, showing a thin layer coating of PANI over VS_2 nanoflakes with minimal destruction of the 3D structure of VS_2. Interestingly, thread-like structures are noticed, inferring nano-wiring of PANI with the VS_2 nanoflakes. Furthermore, the network-induced surface roughness is expected to improve the overall conductivity of the PANI/VS_2

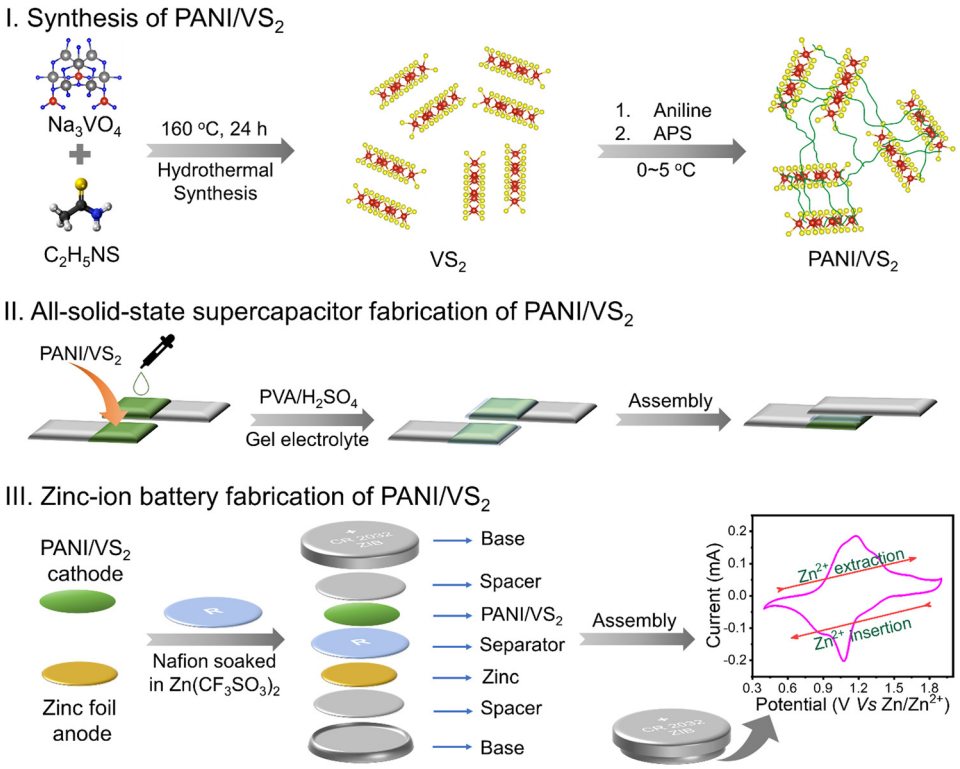

Scheme 1 Schematic presentation of materials synthesis and electrochemical energy device fabrication; (I) the synthesis scheme of the PANI/VS_2 composite material, (II) fabrication of a quasi-solid-state supercapacitor (QSSC) device, and (III) stepwise zinc-ion battery fabrication.

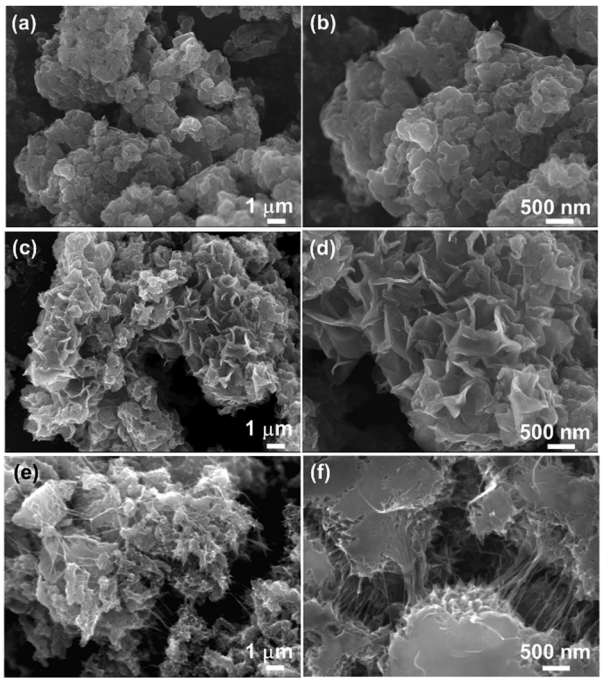

Fig. 1 Field-emission scanning electron microscopy (FESEM) analysis of the prepared materials; (a) and (b) bulk PANI with agglomerated morphology at different magnifications, (c) and (d) the porous layered morphology of VS_2, (e) PANI/VS_2 composite showing the thread-like PANI connected to the VS_2 layers, and (f) magnified image of the PANI/VS_2 composite showing the nanowire-like connections of PANI to the VS_2 layers.

nanocomposite material, enabling it to be suitable for electrochemical applications.

The additional structural information of the PANI/VS_2 composite was obtained from transmission electron microscopy (TEM) analysis (Fig. 2). Fig. 2(a) shows the TEM image of the PANI/VS_2 composite displaying the layered structure of VS_2 along with the PANI network. The inset of Fig. 2(a) shows the low-magnification image of the composite displaying the coexistence of PANI and VS_2. An estimated lattice distance of 0.57 nm stands for the existence of the VS_2 phase (Fig. 2(b)). The observed circular pattern of the selected area electron diffraction (SAED) patterns indicates the amorphous nature of the composite material (Fig. 2(b), inset). In addition, the uniform distribution of PANI nanowires over the VS_2 surface confirms the strong interaction between the two. Furthermore, the uniform distribution of C, N, V, and S elements across the entire area observed in the EDS mapping analysis (Fig. 2(c)–(g)) suggests the coexistence of PANI and VS_2 in the composite structure. The surface area and pore size distribution of the prepared materials were determined by N_2 gas adsorption/desorption analysis (Fig. 3(a) and Fig. S1a, ESI†). The isotherm curves exhibited type IV characteristics, indicating the existence of a mesoporous structure.[26]

Expectedly, 3-dimensional VS_2 nanoflakes displayed the lowest surface area of 35.11 $m^2\ g^{-1}$, mostly contributed by their 3D structure.[27] Despite the agglomerated structure of pristine PANI, it still revealed the largest surface area of 58.5 $m^2\ g^{-1}$ and pore size distribution of 3.07 nm, confirming a mesoporous

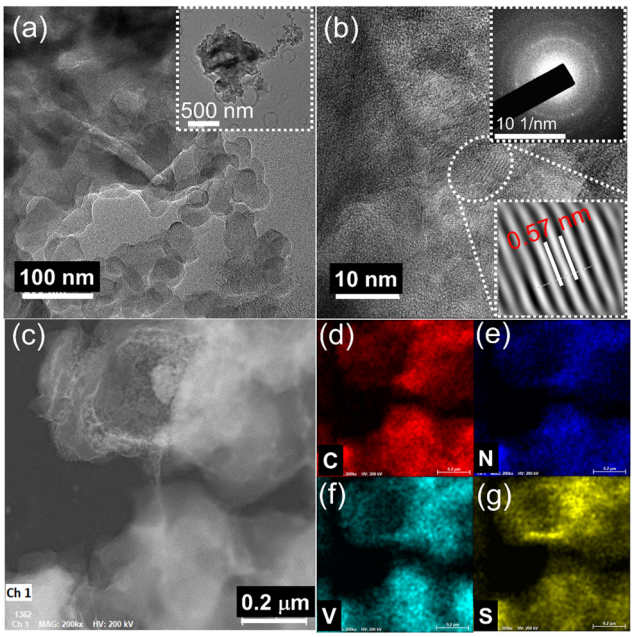

Fig. 2 Transmission electron microscopy (TEM) analysis: (a) TEM image of PANI/VS_2 displaying the VS_2 nanosheets and PANI fibers (inset: low magnification image), (b) high-resolution image of PANI/VS_2 showing the fringes of VS_2 (inset: the SAED pattern); (c) the HAADF STEM image of PANI/VS_2, and (d)–(g) the elemental mapping images displaying the distribution of C, N, V, and S.

structure. Because of the *in situ* growth of PANI on VS_2, the surface area increased in the PANI/VS_2 composite (55.3 m^2 g^{-1}), which is close to that of pristine PANI. Moreover, PANI/VS_2 displayed a relatively narrow pore size distribution with an average pore diameter of 3.8 nm. Interestingly, the PANI/VS_2 composite benefited by incorporating the best properties from either side. Furthermore, the PANI nanowire interconnected structures in the composite enabled a large internal surface area, prompted a more regular hierarchical pore size of the composite, and expanded the contact space between the electrolyte solution and the energy storage material. The content of PANI in the PANI/VS_2 composite was analyzed by TGA as shown in Fig. S1b (ESI†). A small weight loss of ~3 wt% observed before 150 °C is attributed to the loss of surface water. The sharp weight loss between 150 °C and 350 °C in VS_2 is associated with the decomposition of sulfur. The weight loss process occurs in PANI/VS_2 from 150–500 °C, originating from the burning of sulfur and PANI. Therefore, the total PANI content in the PANI/VS_2 composite was estimated to be 40.7 wt%.

The stacked X-ray diffraction (XRD) patterns of VS_2, PANI, and PANI/VS_2 are shown in Fig. 3(b). The diffraction peaks of VS_2 at 15.8° and 36.2° correspond to the (001) and (101) planes of the hexagonal structured VS_2 (JCPDS no. 01-089-1640)[28] and the unassigned peaks in the range of 2θ (20–30°) correspond to the elemental sulfur (JCPDS no. 00-024-0733). However, in the PANI/VS_2 composite, the diffraction peaks for VS_2 were relatively suppressed, ascribed to the high loading of amorphous PANI. The characteristic well-resolved diffraction peaks at 14.8 (011), 21.0 (020), and 25.6 (200) for PANI are visible in the PANI/VS_2 composite.[29] Furthermore, VS_2, PANI, and the PANI/VS_2 composite were analyzed by Raman spectroscopy, as shown in Fig. 3(c). The Raman spectrum of VS_2 showed five peaks at 140.4, 282.0, 406.6, 687.8, and 993.2 cm^{-1}, corresponding to the rocking and stretching vibrations of V–S bonds or their combination.[16] After growing PANI over VS_2, several new peaks appeared, corresponding to the coated PANI in the composite. The observed peaks at 414 and 518 cm^{-1} are assigned to the out-of-plane bending of the PANI rings. The peaks at 582 and 811 cm^{-1} are characteristics of the benzenoid ring deformation and out-of-plane vibrations of aromatic rings, respectively. The observed peaks at 1166, 1223 and 1257, 1336, 1484, 1589, and 1626 cm^{-1} correspond to the C–H, C–N, C–N^+, C═N (di-imine units), C═C, and C–C, respectively.[30] The obvious presence of the PANI peaks in PANI/VS_2 supports the idea that PANI nanowires are uniformly grown covering the entire surface of the VS_2 nanoflakes.

The structural properties and composition of VS_2 and the PANI/VS_2 composite are confirmed by the X-ray photoelectron spectroscopy (XPS) analysis, as shown in Fig. 3(d)–(f). The XPS analysis of the PANI/VS_2 composite provided information about the composition, chemical state, and possible interactions between VS_2 and PANI. The comparative survey scan XPS spectra of VS_2 and PANI/VS_2 (Fig. 3(d)) showed the existence of C, N, O, V, and S elements. The C, N, and O peaks mainly arise from PANI, whereas V and S are contributed by VS_2. The deconvoluted V 2p spectra (Fig. 3(e)) showed the presence of V^{4+} peaks in the range of binding energy (BE) (512–528 eV). The observed peaks of VS_2 at BEs of 517.1 and 524.5 eV correspond to the V $2p_{3/2}$ and V $2p_{1/2}$ of V^{4+}, showing that V^{4+} species are dominant components which are slightly shifted to 516.3 eV and 523.6 eV in the case of PANI/VS_2. In addition, the two peaks at BEs of 513.9 and 521.6 eV are attributed to the V–N bond formed due to the anchoring of polyaniline at VS_2.[21,31] A noticeable shift in the BE of V peaks observed for pristine VS_2 and PANI/VS_2 validates strong electronic interaction between the VS_2 and PANI in the synthesized composite material. In the high-resolution XPS spectrum of S 2p in the PANI/VS_2 composite (Fig. 3(f)), the major peaks are located at 162.6 ($2p_{3/2}$) and 163.8 ($2p_{1/2}$), which show a small shift in BE compared to S 2p peaks of pristine VS_2 at 162.5 ($2p_{3/2}$) and 163.7 eV ($2p_{1/2}$) of S^{2-}. The peaks at 161.6 and 167.2 eV are due to the $S^{2-}2p_{3/2}$ and C–SO_x–N respectively, confirming the interaction between VS_2 and PANI.[21,32] The above physical characterization of the prepared materials validates that the PANI nanowires are uniformly coated on the surface of VS_2. The interaction between PANI nanowires and VS_2 provides excellent interfacial contact and is expected to improve the electrochemical performances in electrochemical energy devices.

2.2. Electrochemical characterization

The electrochemical performance of the resulting materials was evaluated by fabricating the supercapacitor and the ZIBs. For the evaluation of materials and energy devices, various electrochemical techniques were used, including cyclic voltammetry (CV), galvanostatic charge–discharge (GCD), electrochemical

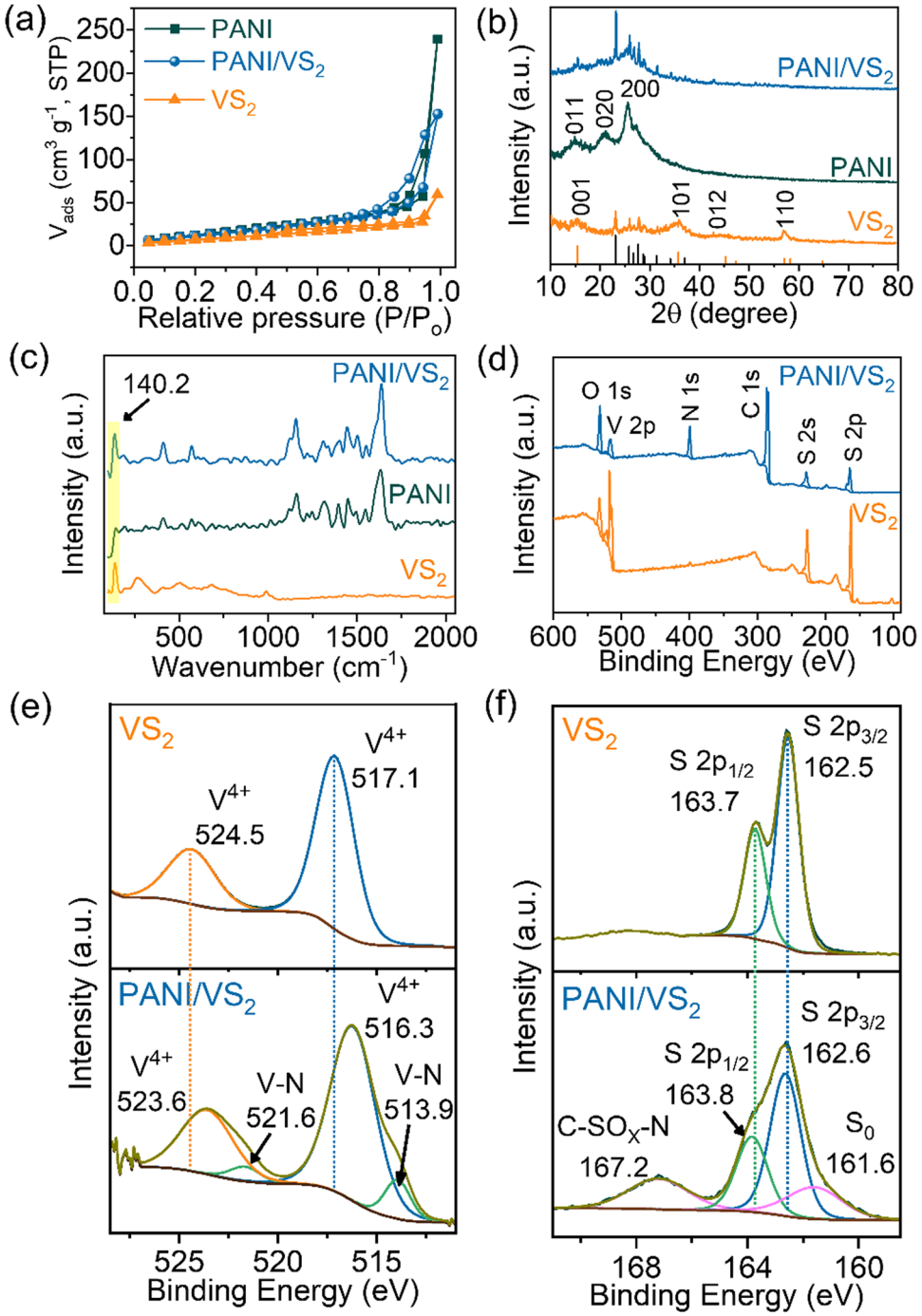

Fig. 3 Physical characterization of the prepared materials: (a) BET surface area analysis of VS_2, PANI and PANI/VS_2; (b) comparative powder X-ray diffraction analysis of VS_2, PANI, and the PANI/VS_2 composite (black color: elemental sulfur; orange color: VS_2); (c) Raman spectra of the materials; (d) survey scan XPS spectra of the PANI/VS_2 composite; and (e) and (f) deconvoluted XPS spectra of V 2p and S 2p respectively.

impedance spectroscopy (EIS), *etc.* First, the perspective of the prepared materials (VS_2, PANI, and PANI/VS_2) towards supercapacitor application was evaluated by measuring the capacitance in 0.5 M H_2SO_4, a liquid state 3-electrode system. The comparative CV analysis of the materials showed (Fig. S2a, ESI†) that the control samples (VS_2 and PANI) exhibited a charge storage capacity (94 and 217 F g^{-1}, at a scan rate of 5 mV s^{-1}).

Furthermore, the layered VS_2 showed a dominant double-layer capacitive behavior as compared to the characteristic pseudocapacitive nature of PANI. On the other hand, the composite material (PANI/VS_2) displayed both the double layer (EDLC) and pseudocapacitance, which overall increases the charge storage capacity (614 F g^{-1}) of the electrode active materials. A similar increasing trend of capacitance was observed for VS_2, PANI, and PANI/VS_2 as measured from the

CD curve as 94, 156, and 822 F g^{-1}, respectively, at a discharge rate of 2 A g^{-1} (Fig. S2b, ESI†).

The observed higher capacitance for the PANI/VS_2 composite material was credited to the higher surface area, supporting that VS_2 prevented the aggregation of PANI fibers while PANI micro-fibers avoided restacking the VS_2 layers, thus improving the overall electronic conductivity. Considering the superior charge storage capacity of PANI/VS_2, detailed electrochemical studies were carried out for the PANI/VS_2-based electrodes. Also, the interfacial cavities created by hetero-bonds and van der Waals interactions may provide the interface to store more ions and provide channels for faster ion migration.[33] The CV studies of the 3-electrode configuration showed a symmetric and stable behavior even at higher scan rates (Fig. S2c, ESI†). The CV recorded at various scan rates (5, 10, 20, 50, and 100 mV s^{-1}) displayed a well-resolved redox peak corresponding to PANI, which revealed that PANI/VS_2 has excellent pseudocapacitive behavior with respective discharge capacitance of 614, 500, 424, 349 and 298 F g^{-1}. The observed symmetric anodic and cathodic redox peaks arise from the transformation of PANI from leucoemeraldine to emeraldine and from emeraldine to pernigraniline, further reflecting the superior reversibility of the capacitive material (PANI/VS_2). The observed capacitance values were 822, 615, 485, 360, and 300 F g^{-1} at variable galvanostatic charge–discharge (GCD) rates of 2, 3, 5, 10, and 20 A g^{-1} (Fig. S2d, ESI†). The changes in capacitance at higher scan and discharge rates are attributed to the faster mobility and sweeping of the ions, which restricts the complete accessibility of the porous surface.

The detailed electrochemical performance of the PANI/VS_2 material was evaluated by employing it in more realistic electrochemical capacitors, *i.e.*, 2-electrode configuration. The two-electrode capacitance under liquid state was measured using a PANI/VS_2 coated electrode as the anode and cathode employing 0.5 M H_2SO_4 as an electrolyte. In a 2-electrode system, the capacitance observed was lower than in a 3-electrode, which is credited to the lack of controlled potential with respect to the reference electrode used in a 3-electrode configuration. Moreover, the indistinguishable redox peaks appeared in the CV measurement (Fig. S2e, ESI†) at different rates (5, 10, 20, 50, and 100 mV s^{-1}), also reflected in the observed capacitance values of 132, 118, 106, 82, and 60 F g^{-1}, respectively (Fig. S2f, ESI†).

Quasi-solid-state supercapacitor (QSSC) device fabrication is an effective way to determine the potential of electrode materials in the real device. The QSSC device was fabricated using PVA:H_2SO_4 as a quasi-solid electrolyte gel and PANI/VS_2 as an active electrode material. The recorded CV of the QSSC device showed a symmetric behavior (Fig. 4(a)) with the capacitance values of 102, 86, 76, 50, and 36 F g^{-1} at different scan rates of 5, 10, 20, 50, and 100 mV s^{-1}, respectively. A similar trend of capacitance is reflected in the capacitance measured from the discharge curve of GCD at galvanostatic rates of 1, 2, 3, and 5 A g^{-1}, as shown in Fig. 4(b). It should be noted that the specific capacitance of the 2-electrode system observed in the liquid electrolyte is close to the capacitance of PANI/VS_2 observed in QSSC devices. Therefore, an effective electrode/electrolyte interface establishment in the QSSC devices is demonstrated, as reflected in the measured equivalent series resistance (ESR) observed in EIS analysis (Fig. 4(c)). In addition, the Nyquist plot of the fabricated QSSC device has shown a very small equivalent resistance of <1.6 ohm with a smaller charge

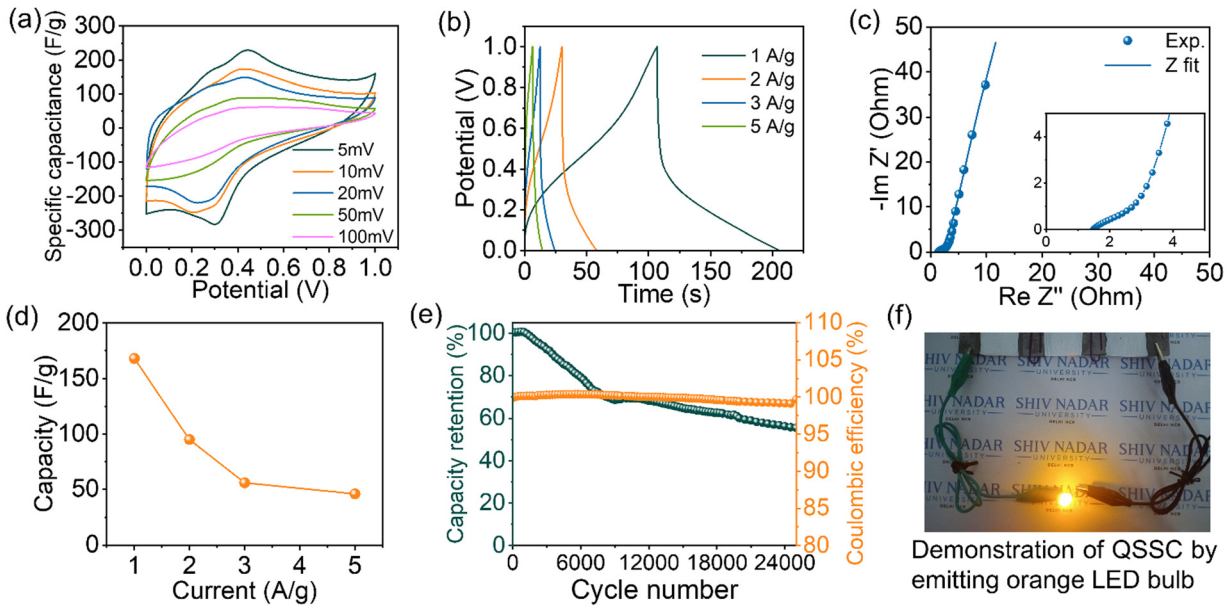

Fig. 4 Electrochemical performances of a quasi-solid-state-supercapacitor (QSSC) device fabricated with the PANI/VS_2 composite; (a) CV curve recorded at a scan rate of 5 to 100 mV s^{-1}, (b) GCD curves at 1 A g^{-1} to 5 A g^{-1}, (c) Nyquist plot showing the ESR and charge transfer resistance, (d) specific capacitance of the device recorded at various current densities of 1, 2, 3, and 5 A g^{-1}, (e) the cycling durability analysis for 25 000 cycles at 10 A g^{-1} and (f) optical image of the demonstration of the QSSC device.

transfer resistance (R_{CT}) of <1.4 ohm. The capacitance of the fabricated QSSC device was measured at various charge–discharge rates (1, 2, 3, and 5 A g^{-1}) to understand the ionic mobility and charge storage capacity in the quasi-solid-state device (Fig. 4(d)). A reduction in the capacity from 168 F g^{-1}@1.0 A g^{-1} to 46 F g^{-1}@5.0 A g^{-1} was observed. The charge storage capacity reduction at a higher scan rate is due to the faster sweeping of ions during the charge–discharge process as observed in the 3-electrode studies (Fig. S5b, ESI†). The durability of the QSSC device was evaluated to check its robustness under operating conditions. The galvanostatic charge–discharge was carried out for 25 000 cycles at 10 A g^{-1} (Fig. 4(e)). The QSSC device has shown a reduction in capacitance ($\sim$28%) after the initial 7700 cycles and a final reduction to 42% after 25 000 cycles with 100% retention in the coulombic efficiency. To investigate the stability of the QSSC, a floating test was carried out at 1 A g^{-1} with a holding period of 2 h after every consecutive 5 cycles of galvanostatic charge–discharge (Fig. S3, ESI†). An $\sim$68% retention in the specific capacitance is obtained. The floating test showed a similar trend in the durability of the QSSC device as observed in galvanostatic charge–discharge cycles between predefined upper and lower voltage cut-off limits (performed at 10 A g^{-1}). The post-mortem analysis of the QSSC devices was carried out after the cycling durability. An agglomeration of the active materials is observed in the SEM image (Fig. S4, ESI†). The agglomeration of the active electrode materials is mainly responsible for the degradation in the charge storage capacity of the fabricated devices as reflected in the durability performance studies. The displayed retention in the capacitance and coulombic efficiency of the fabricated QSSC device shows the potential of the PANI/VS_2 composite toward electrochemical capacitance application.

In addition, the potential of the fabricated QSSC was tested by demonstrating the lighting of LED. One QSSC device gives 1 V, therefore to light the LED, three devices were connected in series resulting in 3 V being able to light the 3 V LED, as illustrated in Fig. 4(f). The observed capacitance of the fabricated QSSC device showed the potential application of PANI/VS_2 toward charge storage.

Furthermore, the zinc-ion battery (ZIB) coin cell testing verified the superior charge storage capacity of the prepared PANI/VS_2 composite. The ZIB was fabricated using Zn foil, PANI/VS_2, and H^+/Zn^{2+} doped Nafion® as the anode, cathode, and separator/electrolyte membrane, respectively (Experimental section). Fig. 5(a) displays the CV curve of the PANI/VS_2 cathode coin cell recorded at scan rate of 0.1 mV s^{-1}. The difference in the CV profile of the initial cycle to the later cycles is related to the gradual activation of the electrode and facilitating the mobility of ions at the electrode/electrolyte interfaces and the intercalation/de-intercalation. In the anodic scan, the prominent oxidation peaks at 1.06 V and 1.19 V *vs.* Zn^{2+}/Zn correspond to the insertion of Zn^{2+} ions into the cathode.

Similarly, in the cathodic scan, the peaks at 1.07 and 0.88 V are attributed to the gradual extraction of Zn^{2+} from the PANI/VS_2. The employment of an H^+ doped Nafion® electrolyte membrane added the advantage of the H^+ shuttle mechanism in the charge–discharge process of the ZIB. Instead of traditional Zn^{2+} ion insertion/extraction, the H^+/Zn^{2+} is known to enhance the performance of ZIBs.[34] The redox peaks at 1.07 and 0.88 V *vs.* Zn^{2+}/Zn correspond to the proton intercalation/extraction, which also facilitates the mobility of Zn^{2+} ions. However, the mechanisms of H^+ ion participation are still not fully understood. The insertion/proton adsorption sites in the cathode are still unknown in the ZIB mechanism.

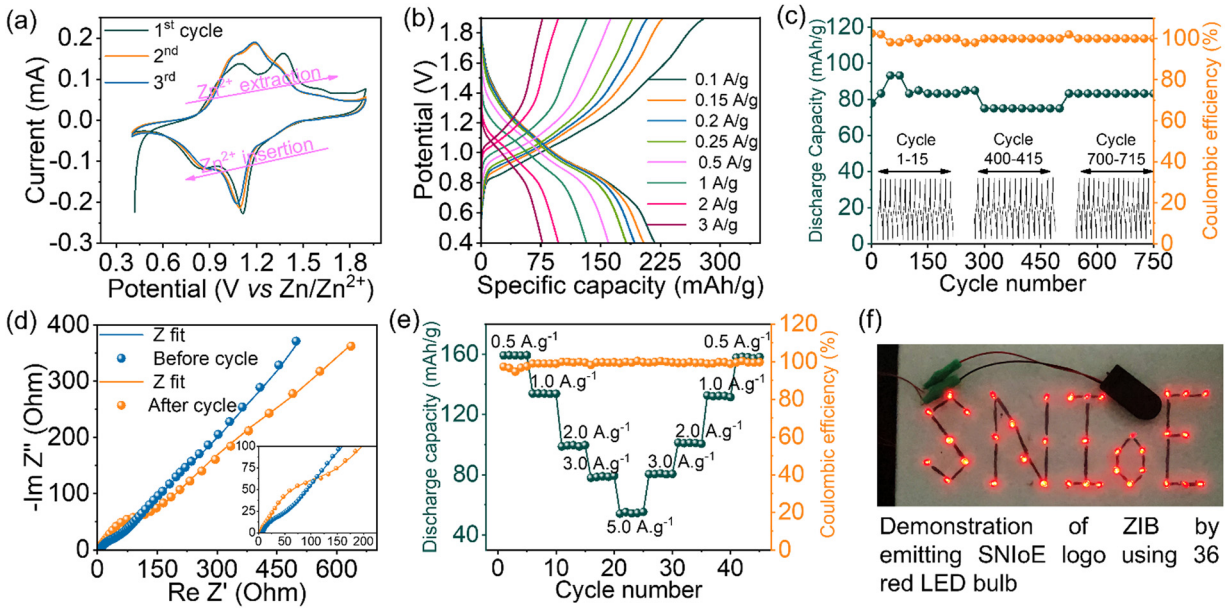

Fig. 5 Electrochemical analysis of the zinc-ion battery coin cell fabricated with PANI/VS_2. (a) CV profile recorded at 0.1 mV s^{-1} scan rate, (b) GCD curve of the ZIB at various current rates, (c) cycling stability data recorded at a GCD current rate of 3.0 A g^{-1}, (d) Nyquist plot recorded before and after the cycling stability test, (e) rate capability plot recorded at different current densities, and (f) device demonstration by emitting red LED.

The impedance analysis (Fig. 5(d), blue curve) of the cell after initial CV cycles displayed a small equivalent series resistance (7 ohm) along with a smaller R_{CT} (85 ohm), validating the effective ion transport.

The galvanostatic charge–discharge (GCD) of the coin cell was performed at different charge–discharge rates (0.10, 0.15, 0.20, 0.25, 0.50, 1.00, 2.00, and 3.00 A g^{-1}) in the accepted potential window as shown in Fig. 5(b). The peaks in the GCD curve at various voltages correspond to the observed redox peaks in the CV analysis. The GCD profile of the PANI/VS_2 cell showed a significantly high discharge capacity of 219 mA h g^{-1} at a discharge rate of 0.1 A g^{-1}. Notably, the discharge capacity of the cell remains considerably high at increased discharge rates of 1, 2, and 3 A g^{-1} suggesting the higher cycling potential of the PANI/VS_2 composite. The discharge curve obtained in the GCD analysis did not reveal a sharp voltage discharge plateau, which might be due to the porous nature of the PANI/VS_2 composite resulting from the prevented stacking and agglomeration of the materials employed. The observed discharge capacity of the PANI/VS_2 cell is comparable or even superior to most of the previously reported performance of ZIBs (Table S1, ESI†).

Furthermore, the charge–discharge long-term durability of the PANI/VS_2 coin cell was evaluated by cycling at 3.0 A g^{-1} for 750 cycles (Fig. 5(c)). The GCD cycle of the cell at 3.0 A g^{-1} showed almost 100% retention in the discharge capacity with an insignificant change in the capacity between the initial ($\sim$80 mA h g^{-1}) and the final GCD cycles ($\sim$79 mA h g^{-1}). The observed small loss in the capacity might be due to the development of resistant layers of $Zn(OH)_2$/ZnO dendrite formation after long cycle durability. The capacity increase in the initial cycles (1–50 cycles) is ascribed to the improved mobility of the ions because of the electrochemical activation of the electrodes. The observed changes in the discharge capacity during the 280–450 cycles is due to variation in temperature during day and night analysis. In addition, the 100% coulombic efficiency retention shows the effective Zn^{2+} ion insertion/extraction during the cycling process. Additionally, the cycling stability data showed $\sim$73% capacity compared to the maximum capacity at 0.5 A g^{-1}. The charge storage capacity during the cyclic durability because of dendrite formation is verified by the EIS analysis, as shown in Fig. 5(d). The comparative Nyquist plot of the PANI/VS_2 cell before and after the durability test shows an increase in R_{CT} from 85 ohm to 204 ohm. The increased R_{CT} of the cell after durability analysis clearly validates the restricted mobility of ions due to the formation of a high resistance layer, which was further verified by the post-analysis of the electrodes (Fig. 6).

The recycling rate capability of the cathode and the capacities of the cell were recorded at various charge–discharge rates in a reversible manner. As shown in Fig. 5(e), the cell showed discharge capacities of 159, 133, 99, 78, and 55 mA h g^{-1} at current rates of 0.5, 1.0, 2.0, 3.0, and 5.0 A g^{-1}, respectively. Furthermore, on decreasing the GCD rate reversibly from 5.0 to 0.5 A g^{-1}, the discharge capacity recovered in the same pattern. However, the slight difference in the discharge capacity is due to the developed resistance, as observed in the EIS analysis (Fig. 5(d)). Notably, the cell showed a 100% retention in coulombic efficiency during charge–discharge cycles at various GCD rates, suggesting the reversible Zn^{2+} ion insertion/extraction process. Considering the 1.5 V supply from one cell observed in the CV and GCD analysis, the two cells connected in series (3.0 V) were directly used for lighting 36 red LEDs connected in parallel arrangement (Fig. 5(f) and Video S1, ESI†).

The post-durability analysis of the anode and cathode of the ZIB coin cell was carried out by FESEM analysis to verify the structural changes of materials responsible for lowering the durability. Fig. 6 shows the FESEM images of the anode and cathode at various magnifications. The FESEM image of the Zn anode (Fig. 6(a)) before the cycling and (Fig. 6(b) and (c)) after the durability test shows the generation of dendrites on the surface, which also causes the development of passivation

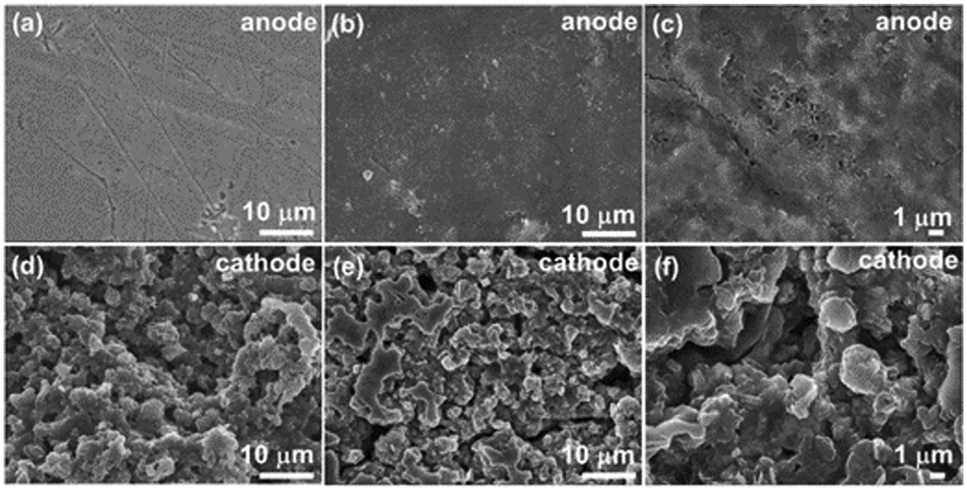

Fig. 6 FESEM analysis of the anode and cathode materials of a coin cell after 750 charge–discharge cycles: (a)–(c) FESEM images of the zinc anode and (d)–(f) FESEM images of the PANI/VS_2 cathode.

layers responsible for increased resistance as observed in the EIS analysis (Fig. 5(d)). In contrast, the FESEM images of the PANI/VS_2 cathode (Fig. 6(d)) before and after cycling test (Fig. 6(e) and (f)) display no change in the structural behavior, validating the robustness of the prepared electrode material.

3. Conclusions

In summary, we have developed a PANI/VS_2 composite material using a facile and effective route. The introduction of VS_2 not only induced a uniform dispersion of PANI on its surface but also resulted in a nano-wiring effect between the components. The latter yields a PANI/VS_2 composite with improved electrochemical properties. A quasi-solid-state supercapacitor device was fabricated using PANI/VS_2 electrodes with the aid of a PVA–H_2SO_4 gel electrolyte. The stable cyclic behavior and higher specific capacity of the formed QSSC clearly support the well-matured component of the designed QSSC device. In addition, it also serves as an excellent host for the reversible insertion/extraction of the Zn^{2+} ions, delivering 219 mA h g^{-1} capacity at 0.1 A g^{-1}. Using a Nafion® ionomer membrane stabilizes the anode in a Zn//PANI/VS_2 cell by suppressing the growth of bulk/dendritic Zn deposits at the cathode during cycling. The charge–discharge long-term durability of the PANI/VS_2 coin cell at 3.0 A g^{-1} for 750 cycles displays the robustness of the composite material as an electrode. The developed material has great potential towards large-scale energy storage applications because of its low-cost, safety, and environmental friendliness.

4. Experimental section

4.1 Materials

Sodium orthovanadate (Na_3VO_4, 99%), thioacetamide (TAA, 99%), aniline (99.5%), ammonium persulfate (98%), zinc trifluoromethanesulfonate [Zn–$(CF_3SO_3)_2$], polyvinyl alcohol (PVA), sulfuric acid (H_2SO_4, 98%), hydrochloric acid (HCl, 36.5%), *N*-methyl-2-pyrrolidone (NMP), and methanol were procured from Sigma Aldrich and used without further purification. Grafoil® paper and Toray carbon were procured from Fuel Cell Store, USA. Nafion®-212 was procured from DuPont, USA.

4.2 Synthesis of VS_2

In a typical synthesis, 17.5 mmol thioacetamide (C_2H_5NS) was added to 70 ml of methanol and stirred at room temperature for 30 min before the addition of 3.5 mmol sodium orthovanadate (Na_3VO_4). The mixed solution was transferred to a Teflon-lined stainless-steel autoclave with a capacity of 100 ml. The autoclave was sealed and maintained at 160 °C for 24 h. The obtained product was thoroughly washed with deionized water and absolute alcohol several times and dried in a vacuum oven at 60 °C for 8 h.

4.3 Synthesis of the PANI/VS_2 composite

For the preparation of the composite material, first, VS_2 (62.5 mg) was bath sonicated in 20 ml of deionized water for 1 h to get a well-dispersed VS_2 solution. Separately, a solution of aniline (0.57 ml) in HCl (1.93 ml) was prepared and stirred in 8.5 ml of deionized water for 45 min. The mixture solution was slowly added dropwise to the VS_2 dispersion and stirred for 1 h to get a well-dispersed aniline solution on the VS_2 nanosheets. Subsequently, a solution of APS (0.1 M, 13 ml) was added quickly to the aniline–VS_2 reaction mixture and continually agitated with a magnetic stirrer at 4 °C for 4 h. After completion of the reaction, the PANI/VS_2 composite was collected from the solution by filtration and vacuum dried at 60 °C for 6 h. For comparison, pristine PANI was also synthesized with the same procedure without adding VS_2.

4.4 Characterization

The surface morphology and elemental mapping of the copolymer were examined using a field emission scanning electron microscope (FESEM), Jeol JSM-7610Plus coupled with an energy-dispersive X-ray (EDX, AMETEK) detector, under an acceleration voltage of 15 kV. Transmission electron microscopy (TEM) images were recorded using an HRTEM, JEOL-2100F instrument under an accelerating voltage of 200 kV, and the *d*-spacing was calculated using GATAN software. Powder X-ray diffraction (PXRD) was carried out using a Bruker D8 diffractometer, using Cu Kα (λ = 1.5406 Å) in the scattering range (2θ) of 10–80° at room temperature. Thermogravimetric analysis (TGA) was performed with a built-in gas controller (TGA2 SF/1100) and fitted with an XP1U TGA balance (ultra-microbalance) under a 50 ml min^{-1} flow rate of nitrogen and zero air in the temperature range of 35–800 °C at a heating rate of 10 °C min^{-1}. Raman spectroscopy measurements were carried out with an STR500 Airix microscope using a 532 nm laser at a power of 3 mW. X-ray photoelectron spectroscopy (XPS) measurements were carried out using a Thermo Fisher NEXSA surface analyzer with a monochromatized Al Kα (1486.7 eV) radiation source to determine the chemical composition and binding energies (BEs). The acquired spectrum was charge-corrected at a BE of carbon 1s peak at 284.6 eV and processed with the CasaXPS software. The porosity and surface area were determined using the Brunauer–Emmer–Teller (BET) method (Nova Touch LX2, Quantachrome).

4.5 PVA–H_2SO_4 gel preparation

The electrolyte gel was prepared by adding about 2 g of PVA to 20 ml of Millipore water and stirring at 80 °C until the solution became clear. The clear solution was cooled to room temperature, and 2 g of concentrated H_2SO_4 (98%) was added dropwise with continuous stirring and mixing for 30 min. The obtained electrolyte was 10 wt%, 1 : 1 PVA : H_2SO_4 gel used for the QSSC device fabrication.

4.6 Fabrication of quasi-solid-state supercapacitors

For the QSSC fabrication, PANI/VS_2 was prepared by mixing 95% active material with 5% Nafion® in NMP. Furthermore, ~1.1 mg of the material was coated onto the surface of a 1 × 1 cm^2 area of a Grafoil® sheet (thickness ~0.46 mm). For the electrode preparation, the Grafoil with the dimension of

1×3 cm^2 was selected; the excess area was used as the current collector contact during the measurements. The above electrodes were dried in a vacuum oven at 60 °C overnight. The dried electrode's active material coated area was further coated with a thin film of the PVA:H_2SO_4 gel and the two electrodes were sandwiched to make the device where a membrane was used as a separator.

4.7 Pretreatment of the Nafion® ionomer membranes

Prior to use of the Nafion® ionomer membrane (Nafion® 212) in the zinc-ion battery assembly, the Nafion® membrane was treated sequentially at 80 °C for 30 min in (i) 4 wt% H_2O_2; (ii) DI water; (iii) 0.8 M H_2SO_4; and (iv) DI water, respectively, where the numbers represent the order of treatment. The obtained pre-treated Nafion® ionomer membrane (thickness ~60 μm) was dipped in a 1 M [$Zn(CF_3SO_3)_2$] electrolyte salt concentration for 2 days to get soaked with a sufficient amount of Zn^{2+}.

4.8 Assembly of the Zn//PANI/VS_2 full cell

All the Zn//PANI/VS_2 cells were assembled in the CR2032 coin cell in a traditional fashion, where a zinc foil (diameter = 11.3 mm, weight = 0.33 g and thickness = 0.40 mm), a freshly prepared PANI/VS_2 electrode (diameter = 11.3 mm, 1.1 PANI/VS_2 mg in 1 cm^2), and the desired Nafion® ionomer membrane (diameter = 15.5 mm), presoaked in an aqueous [$Zn(CF_3SO_3)_2$] electrolyte, were used as the anode, cathode, and separator, respectively. Here, the terms anode and cathode are used for the negative and positive electrodes, respectively, considering the discharge state of the cell.

4.9 Electrochemical measurements

The three-electrode configuration cell connected to the electrochemical workstation (BioLogic VMP3) was used to analyze the electrochemical performance through a series of electrochemical measuring techniques: cyclic voltammetry (CV), galvanostatic charge/discharge (GCD), and electrochemical impedance spectroscopy (EIS). This cell included the electrolyte solution (0.5 M H_2SO_4), counter electrode (Toray carbon), reference electrode (Ag/AgCl electrodes), and the working electrode (mass: 1.05 mg cm^{-2}).

The capacitance of the working electrode was evaluated with the equation:

$$C = \frac{\int_{V1}^{V2} I(V)\mathrm{d}V}{V \times \frac{\mathrm{d}V}{\mathrm{d}t}}, \quad C_G = 2\frac{C}{M}$$

where C_G is the gravimetric capacitance of the electrode active material. Note that these are specific capacitances by definition; $\int_{V1}^{V2} I(V)\mathrm{d}V$ is the average current from the anodic or cathodic sweep, V is the potential window (in volts), A is the active area per electrode (in cm^2), M is the active mass per electrode (in grams), and $\mathrm{d}V/\mathrm{d}t$ is the scan rate (mV s^{-1}).

For CD, the equation is:

$$C = \frac{I_{\text{discharge}}}{\mathrm{d}V/\mathrm{d}t}, \; C_G = 2\frac{C}{M}$$

where $I_{\text{discharge}}$ is the discharge current (in mA), $\mathrm{d}V/\mathrm{d}t$ is the slope of the discharge curve (in V s^{-1}), and M is the active mass per electrode (in grams).

The capacity of the Zn//PANI/VS_2 is calculated from the galvanostatic charge–discharge plot using the equation:

$$\text{Capacity} = \text{Discharge time (h)} \times \text{applied current density (A g}^{-1}) \times 1000.$$

Author contributions

The manuscript was written through the contributions of all authors. All authors approved the final version of the manuscript.

Conflicts of interest

There are no conflicts to declare.

Acknowledgements

The authors acknowledge the financial support from the Shiv Nadar Foundation and Shiv Nadar Institution of Eminence. The authors would like to acknowledge IISER, Mohali, for recording the TEM data, and Scientium Analyze Solutions for the characterization.

References

1 B. Dunn, H. Kamath and J.-M. Tarascon, Electrical energy storage for the grid: a battery of choices, *Science*, 2011, **334**(6058), 928–935, DOI: **10.1126/science.1212741**; D. Larcher and J.-M. Tarascon, Towards greener and more sustainable batteries for electrical energy storage, *Nat. Chem.*, 2015, **7**(1), 19–29, DOI: **10.1038/nchem.2085**; P. Yang and J.-M. Tarascon, Towards systems materials engineering, *Nat. Mater.*, 2012, **11**(7), 560–563, DOI: **10.1038/nchem.2085**.

2 J. Bai, X. Li, G. Liu, Y. Qian and S. Xiong, Unusual Formation of $ZnCo_2O_4$ 3D Hierarchical Twin Microspheres as a High-Rate and Ultralong-Life Lithium-Ion Battery Anode Material, *Adv. Funct. Mater.*, 2014, **24**(20), 3012–3020, DOI: **10.1002/adfm.201303442**; Y. Meesala, A. Jena, H. Chang and R.-S. Liu, Recent Advancements in Li-Ion Conductors for All-Solid-State Li-Ion Batteries, *ACS Energy Lett.*, 2017, **2**(12), 2734–2751, DOI: **10.1021/acsenergylett.7b00849**.

3 J. B. Goodenough and Y. Kim, Challenges for Rechargeable Li Batteries, *Chem. Mater.*, 2010, **22**(3), 587–603, DOI: **10.1021/cm901452z**; V. Etacheri, R. Marom, R. Elazari, G. Salitra and D. Aurbach, Challenges in the development of advanced Li-ion batteries: a review, *Energy Environ. Sci.*, 2011, **4**(9), 3243–3262, DOI: **10.1039/C1EE01598B**.

4 W. Chen, C. Xia and H. N. Alshareef, One-Step Electrodeposited Nickel Cobalt Sulfide Nanosheet Arrays for High-Performance Asymmetric Supercapacitors, *ACS Nano*,

2014, **8**(9), 9531–9541, DOI: 10.1021/nn503814y; C. Deng, S. Zhang, Z. Dong and Y. Shang, 1D nanostructured sodium vanadium oxide as a novel anode material for aqueous sodium ion batteries, *Nano Energy*, 2014, **4**, 49–55, DOI: 10.1016/j.nanoen.2013.12.014; M. Pasta, C. D. Wessells, N. Liu, J. Nelson, M. T. McDowell, R. A. Huggins, M. F. Toney and Y. Cui, Full open-framework batteries for stationary energy storage, *Nat. Commun.*, 2014, **5**(1), 1–9, DOI: 10.1038/ncomms4007; W.-J. Song, S. Lee, G. Song and S. Park, Stretchable Aqueous Batteries: Progress and Prospects, *ACS Energy Lett.*, 2019, **4**(1), 177–186, DOI: 10.1021/acsenergylett.8b02053; T. Liu, H. Wu, X. Du, J. Wang, Z. Chen, H. Wang, J. Sun, J. Zhang, J. Niu and L. Yao, *et al.*, Water-Locked Eutectic Electrolyte Enables Long-Cycling Aqueous Sodium-Ion Batteries, *ACS Appl. Mater. Interfaces*, 2022, **14**(29), 33041–33051, DOI: 10.1021/acsami.2c04893.

5 Y. Wang, J. Liu, B. Lee, R. Qiao, Z. Yang, S. Xu, X. Yu, L. Gu, Y. Hu and W. Yang, Ti-substituted tunnel-type Na0.44MnO2 oxide as a negative electrode for aqueous sodium-ion batteries, *Nat. Commun.*, 2015, **6**, 6401, DOI: 10.1038/ncomms7401; K.-H. Nam, Y. Hwa and C.-M. Park, Zinc Phosphides as Outstanding Sodium-Ion Battery Anodes, *ACS Appl. Mater. Interfaces*, 2020, **12**(13), 15053–15062, DOI: 10.1021/acsami.9b21803; P. Jiang, Z. Lei, L. Chen, X. Shao, X. Liang, J. Zhang, Y. Wang, J. Zhang, Z. Liu and J. Feng, Polyethylene Glycol–Na^+ Interface of Vanadium Hexacyanoferrate Cathode for Highly Stable Rechargeable Aqueous Sodium-Ion Battery, *ACS Appl. Mater. Interfaces*, 2019, **11**(32), 28762–28768, DOI: 10.1021/acsami.9b04849.

6 Z. Yu, L. Tetard, L. Zhai and J. Thomas, Supercapacitor electrode materials: nanostructures from 0 to 3 dimensions, *Energy Environ. Sci.*, 2015, **8**(3), 702–730, DOI: 10.1039/C4EE03229B; J. Rehman, K. Eid, R. Ali, X. Fan, G. Murtaza, M. Faizan, A. Laref, W. Zheng and R. S. Varma, Engineering of Transition Metal Sulfide Nanostructures as Efficient Electrodes for High-Performance Supercapacitors, *ACS Appl. Energy Mater.*, 2022, **5**(6), 6481–6498, DOI: 10.1021/acsaem.1c03937; D. Kasprzak, C. C. Mayorga-Martinez and M. Pumera, Sustainable and Flexible Energy Storage Devices: A Review, *Energy Fuels*, 2023, **37**(1), 74–97, DOI: 10.1021/acs.energyfuels.2c03217.

7 G. Fang, J. Zhou, A. Pan and S. Liang, Recent advances in aqueous zinc-ion batteries, *ACS Energy Lett.*, 2018, **3**(10), 2480–2501, DOI: 10.1021/acsenergylett.8b01426; Z. Liu, Y. Yang, S. Liang, B. Lu and J. Zhou, pH-Buffer contained electrolyte for self-adjusted cathode-free Zn–MNo_2 batteries with coexistence of dual mechanisms, *Small Struct.*, 2021, **2**(11), 2100119, DOI: 10.1002/sstr.202100119.

8 C. Xu, B. Li, H. Du and F. Kang, Energetic zinc ion chemistry: the rechargeable zinc ion battery, *Angew. Chem., Int. Ed.*, 2012, **124**(4), 957–959, DOI: 10.1002/ange.201106307; D. Kundu, B. D. Adams, V. Duffort, S. H. Vajargah and L. F. Nazar, A high-capacity and long-life aqueous rechargeable zinc battery using a metal oxide intercalation cathode, *Nat. Energy*, 2016, **1**(10), 1–8, DOI: 10.1038/nenergy.2016.119; Y. Song, P. Ruan, C. Mao, Y. Chang, L. Wang, L. Dai, P. Zhou, B. Lu, J. Zhou and Z. He, Metal–organic frameworks functionalized separators for robust aqueous zinc-ion batteries, *Nano-Micro Lett.*, 2022, **14**(1), 218, DOI: 10.1007/s40820-022-00960-z.

9 H. Pan, Y. Shao, P. Yan, Y. Cheng, K. S. Han, Z. Nie, C. Wang, J. Yang, X. Li and P. Bhattacharya, Reversible aqueous zinc/manganese oxide energy storage from conversion reactions, *Nat. Energy*, 2016, **1**(5), 1–7.

10 J. Plawan Kumar, S. Santosh Kumar, K. Vikash, R. Shammi, K. Sreekumar and B. Nirmalya, High-Level Supercapacitive Performance of Chemically Reduced Graphene Oxide, *Chem*, 2017, **3**(5), 846–860, DOI: 10.1016/j.chempr.2017.08.011; X. Yang, H. Wang, Y. Song, K. Liu, T. Huang, X. Wang, C. Zhang and J. Li, Low-Temperature Synthesis of a Porous High-Entropy Transition-Metal Oxide as an Anode for High-Performance Lithium-Ion Batteries, *ACS Appl. Mater. Interfaces*, 2022, **14**(23), 26873–26881, DOI: 10.1021/acsami.2c07576.

11 Y. Li, H. Wang, L. Xie, Y. Liang, G. Hong and H. Dai, MoS_2 nanoparticles grown on graphene: an advanced catalyst for the hydrogen evolution reaction, *J. Am. Chem. Soc.*, 2011, **133**(19), 7296–7299, DOI: 10.1021/ja201269b.

12 H. Hwang, H. Kim and J. Cho, MoS_2 nanoplates consisting of disordered graphene-like layers for high rate lithium battery anode materials, *Nano Lett.*, 2011, **11**(11), 4826–4830, DOI: 10.1021/nl202675f.

13 C. S. Rout, B.-H. Kim, X. Xu, J. Yang, H. Y. Jeong, D. Odkhuu, N. Park, J. Cho and H. S. Shin, Synthesis and characterization of patronite form of vanadium sulfide on graphitic layer, *J. Am. Chem. Soc.*, 2013, **135**(23), 8720–8725, DOI: 10.1021/ja403232d; N. Choudhary, C. Li, H.-S. Chung, J. Moore, J. Thomas and Y. Jung, High-performance one-body core/shell nanowire supercapacitor enabled by conformal growth of capacitive 2D WS_2 layers, *ACS Nano*, 2016, **10**(12), 10726–10735, DOI: 10.1021/acsnano.6b06111; J. R. Dunklin, H. Zhang, Y. Yang, J. Liu and J. van de Lagemaat, Dynamics of Photocatalytic Hydrogen Production in Aqueous Dispersions of Monolayer-Rich Tungsten Disulfide, *ACS Energy Lett.*, 2018, **3**(9), 2223–2229, DOI: 10.1021/acsenergylett.8b01287; D. Sarkar, D. Das, S. Das, A. Kumar, S. Patil, K. K. Nanda, D. D. Sarma and A. Shukla, Expanding Interlayer Spacing in MoS_2 for Realizing an Advanced Supercapacitor, *ACS Energy Lett.*, 2019, **4**(7), 1602–1609, DOI: 10.1021/acsenergylett.9b00983.

14 J. Feng, X. Sun, C. Wu, L. Peng, C. Lin, S. Hu, J. Yang and Y. Xie, Metallic few-layered VS_2 ultrathin nanosheets: high two-dimensional conductivity for in-plane supercapacitors, *J. Am. Chem. Soc.*, 2011, **133**(44), 17832–17838, DOI: 10.1021/ja207176c.

15 J. Park, S. J. Kim, K. Lim, J. Cho and K. Kang, Reconfiguring Sodium Intercalation Process of TiS_2 Electrode for Sodium-Ion Batteries by a Partial Solvent Cointercalation, *ACS Energy Lett.*, 2022, **7**(10), 3718–3726, DOI: 10.1021/acsenergylett.2c01838; H. Zhang, J. Song, J. Li, J. Feng, Y. Ma, L. Ma, H. Liu, Y. Qin, X. Zhao and F. Wang, Interlayer-Expanded MoS_2 Nanoflowers Vertically Aligned on MXene@Dual-Phased TiO_2 as High-Performance Anode for Sodium-Ion Batteries, *ACS Appl. Mater. Interfaces*, 2022, **14**(14), 16300–16309, DOI: 10.1021/acsami.2c02080.

16 P. He, M. Yan, G. Zhang, R. Sun, L. Chen, Q. An and L. Mai, Layered VS_2 nanosheet-based aqueous Zn ion battery cathode, *Adv. Energy Mater.*, 2017, **7**(11), 1601920, DOI: **10.1002/aenm.201601920**.

17 X. Xu, F. Xiong, J. Meng, X. Wang, C. Niu, Q. An and L. Mai, Vanadium-based nanomaterials: a promising family for emerging metal-ion batteries, *Adv. Funct. Mater.*, 2020, **30**(10), 1904398, DOI: **10.1002/adfm.201904398**; L. Hu, J. R. Jokisaari, B. J. Kwon, L. Yin, S. Kim, H. Park, S. H. Lapidus, R. F. Klie, B. Key and P. Zapol, *et al.*, High Capacity for Mg^{2+} Deintercalation in Spinel Vanadium Oxide Nanocrystals, *ACS Energy Lett.*, 2020, **5**(8), 2721–2727, DOI: **10.1021/acsenergylett.0c01189**.

18 J. Feng, L. Peng, C. Wu, X. Sun, S. Hu, C. Lin, J. Dai, J. Yang and Y. Xie, Giant moisture responsiveness of VS2 ultrathin nanosheets for novel touchless positioning interface, *Adv. Mater.*, 2012, **24**(15), 1969–1974, DOI: **10.1002/adma.201104681**; S. Wang, H. Chen, J. Liao, Q. Sun, F. Zhao, J. Luo, X. Lin, X. Niu, M. Wu and R. Li, *et al.*, Efficient Trapping and Catalytic Conversion of Polysulfides by VS4 Nanosites for Li–S Batteries, *ACS Energy Lett.*, 2019, **4**(3), 755–762, DOI: **10.1021/acsenergylett.9b00076**.

19 P. Sekar, B. Anothumakkool and S. Kurungot, 3D polyaniline porous layer anchored pillared graphene sheets: enhanced interface joined with high conductivity for better charge storage applications, *ACS Appl. Mater. Interfaces*, 2015, **7**(14), 7661–7669, DOI: **10.1021/acsami.5b00504**.

20 P. Liu, J. Yan, Z. Guang, Y. Huang, X. Li and W. Huang, Recent advancements of polyaniline-based nanocomposites for supercapacitors, *J. Power Sources*, 2019, **424**, 108–130, DOI: **10.1016/j.jpowsour.2019.03.094**.

21 X. Wang, Y. Zhang, J. Zheng, X. Liu and C. Meng, Hydrothermal synthesis of VS_4/CNTs composite with petal-shape structures performing a high specific capacity in a large potential range for high-performance symmetric supercapacitors, *J. Colloid Interface Sci.*, 2019, **554**, 191–201, DOI: **10.1016/j.jcis.2019.06.105**.

22 P. Yu, X. Zhao, Z. Huang, Y. Li and Q. Zhang, Free-standing three-dimensional graphene and polyaniline nanowire arrays hybrid foams for high-performance flexible and lightweight supercapacitors, *J. Mater. Chem. A*, 2014, **2**(35), 14413–14420, DOI: **10.1039/C4TA02721C**.

23 X. Fu, W. Zhang, B. Lan, J. Wen, S. Zhang, P. Luo, R. Zhang, S. Hu and Q. Liu, Polyaniline Nanorod Arrays as a Cathode Material for High-Rate Zinc-Ion Batteries, *ACS Appl. Energy Mater.*, 2020, **3**(12), 12360–12367, DOI: **10.1021/acsaem.0c02373**.

24 M. J. Park, H. Yaghoobnejad Asl and A. Manthiram, Multivalent-ion versus proton insertion into battery electrodes, *ACS Energy Lett.*, 2020, **5**(7), 2367–2375, DOI: **10.1021/acsenergylett.0c01021**.

25 M. Ghosh, V. Vijayakumar and S. Kurungot, Dendrite growth suppression by Zn^{2+} integrated Nafion® ionomer membranes: beyond porous separators toward aqueous Zn/V_2O_5 batteries with extended cycle life, *Energy Technol.*, 2019, **7**(9), 1900442, DOI: **10.1002/ente.201900442**.

26 X. Li, C. Zhang, S. Xin, Z. Yang, Y. Li, D. Zhang and P. Yao, Facile synthesis of MoS_2/reduced graphene oxide@polyaniline for high-performance supercapacitors, *ACS Appl. Mater. Interfaces*, 2016, **8**(33), 21373–21380, DOI: **10.1021/acsami.6b06762**.

27 J. Zhang, C. Zhang, Z. Wang, J. Zhu, Z. Wen, X. Zhao, X. Zhang, J. Xu and Z. Lu, Synergistic interlayer and defect engineering in VS_2 nanosheets toward efficient electrocatalytic hydrogen evolution reaction, *Small*, 2018, **14**(9), 1703098, DOI: **10.1002/smll.201703098**.

28 D. Yu, Q. Pang, Y. Gao, Y. Wei, C. Wang, G. Chen and F. Du, Hierarchical flower-like VS_2 nanosheets-A high rate-capacity and stable anode material for sodium-ion battery, *Energy Storage Mater.*, 2018, **11**, 1–7, DOI: **10.1016/j.ensm.2017.09.002**.

29 W. Wu, Y. Li, G. Zhao, L. Yang and D. Pan, Aldehyde–poly (ethylene glycol) modified graphene oxide/conducting polymers composite as high-performance electrochemical supercapacitors, *J. Mater. Chem. A*, 2014, **2**(42), 18058–18069, DOI: **10.1039/C4TA03018D**.

30 S. A. Hasoon, Electrochemical polymerization and Raman study of polypyrrole and polyaniline thin films, *Int. J. Phys. Sci.*, 2012, **7**(38), 5468–5476, DOI: **10.5897/IJPS12.529**.

31 Y. Cheng, Y. Shao, V. Raju, X. Ji, B. L. Mehdi, K. S. Han, M. H. Engelhard, G. Li, N. D. Browning and K. T. Mueller, Molecular storage of Mg ions with vanadium oxide nanoclusters, *Adv. Funct. Mater.*, 2016, **26**(20), 3446–3453, DOI: **10.1002/adfm.201505501**; G. Silversmit, D. Depla, H. Poelman, G. B. Marin and R. De Gryse, Determination of the V2p XPS binding energies for different vanadium oxidation states (V^{5+} to V^{0+}), *J. Electron Spectrosc. Relat. Phenom.*, 2004, **135**(2–3), 167–175, DOI: **10.1016/j.elspec.2004.03.004**; R. Manikandan, C. J. Raj, M. Rajesh, B. C. Kim, S. Park and K. H. Yu, Vanadium Pentoxide with H_2O, K^+, and Na^+ Spacer between Layered Nanostructures for High-Performance Symmetric Electrochemical Capacitors, *Adv. Mater. Interfaces*, 2018, **5**(12), 1800041, DOI: **10.1002/admi.201800041**; N. Zhang, L. Cao, L. Feng, J. Huang, K. Kajiyoshi, C. Li, Q. Liu, D. Yang and J. He, Co, N-Codoped porous vanadium nitride nanoplates as superior bifunctional electrocatalysts for hydrogen evolution and oxygen reduction reactions, *Nanoscale*, 2019, **11**(24), 11542–11549, DOI: **10.1039/c9nr02637a**.

32 D. Haldar, S. Bose, A. Ghosh and S. K. Saha, A green luminescent MoS2–CdTe hybrid nanostructure synthesized through surface charge interaction, *Nanoscale Adv.*, 2019, **1**(5), 1853–1863, DOI: **10.1039/C8NA00388B**.

33 Y. Dai, X. Liao, R. Yu, J. Li, J. Li, S. Tan, P. He, Q. An, Q. Wei and L. Chen, *et al.*, Quicker and more Zn(2+) storage predominantly from the interface, *Adv. Mater.*, 2021, **33**(26), e2100359, DOI: **10.1002/adma.202100359**.

34 W. Sun, F. Wang, S. Hou, C. Yang, X. Fan, Z. Ma, T. Gao, F. Han, R. Hu and M. Zhu, Zn/MnO_2 battery chemistry with H^+ and Zn^{2+} coinsertion, *J. Am. Chem. Soc.*, 2017, **139**(29), 9775–9778, DOI: **10.1021/jacs.7b04471**.